Chemical Engineering Journal 534 (2026) 174901

Contents lists available at ScienceDirect

Chemical Engineering Journal

journal homepage: www.elsevier.com/locate/cej

Advancing electrified CO_2 capture: Material design strategies for magnetic adsorption composites

Oliver Stratil [a], Oscar Cespedes [b], Olivier Croquet [c], Thierry Visart de Bocarmé [c], Rafael Gonzalez-Olmos [a], Javier Fernandez-Garcia [a,*]

[a] IQS School of Engineering, Universitat Ramon Llull, Via Augusta 390, 08017, Barcelona, Spain
[b] School of Physics and Astronomy, University of Leeds, Leeds, LS2 9JT, United Kingdom
[c] Chemistry of Surfaces, Interfaces and Nanomaterials, Faculty of Sciences, Université Libre de Bruxelles, Campus Plaine, CP 243, 1050, Bruxelles, Belgium

A B S T R A C T

This study investigates the design and performance of magnetic adsorption composites (MACs) for application in electrified CO_2 capture with temperature swing adsorption from point sources. The MACs were composed of Fe_3O_4 as magnetic component to act as inductive heating source and zeolite 13× as a CO_2 adsorbent. Three MAC configurations were prepared and evaluated under temperature feedback-loop control at different desorption temperatures ranging between $100-150^{\circ}C$: Homogeneous mixture of Fe_3O_4 and zeolite 13×, a core-shell structure with magnetic Fe_3O_4 core and zeolite 13× shell, and a mixed bed configuration containing separate heating and adsorbent beads. Resistive wall heated and room-temperature desorption experiments were conducted as references. In average, the heating experiments reached a steady-state effective working capacity after around 20 adsorption-desorption cycles. The homogenous mixture exhibited the most favorable performance, combining fast heating response, stable temperature control, and high CO_2 desorption efficiency. When reaching steady state, it achieved 99% desorption within 94 s and the highest productivity of 0.52 $\frac{mg_{CO_2}}{g_{MAC} \bullet s}$ with a theoretical regeneration energy of 3.0 $\frac{MJ}{kg_{CO_2}}$. The core-shell structure showed limited temperature control due to low heat transfer through the shell, while the mixed bed configuration achieved moderate performance. Compared with column wall heating, inductive heating improved thermal efficiency by delivering heat directly to the adsorbent region. However, efficient coupling of the magnetic field to the magnetic material remains the key challenge for energy efficient induction heated TSA.

Abbreviations

Abbreviations	**Description**
ads	Adsorbed
BET	Brunauer-Emmett-Teller
CMC	Carboxymethyl cellulose
CMS	Carbon molecular sieve
CS	Core-Shell
des	Desorbed
el	Electrical
Fe_3O_4	Magnetite
HG	Homogeneous
IH	Induction heating
MAC	Magnetic adsorption composite
max	Maximum
MB	Mixed bed
$MgFe_2O_4$	Magnesium ferrite
MOF	Metal-organic framework
reg	Regeneration
RT	Room temperature
SAR	Specific absorption rate
SM	Supplementary Material
SQUID-VSM	Vibrating Sample magnetometry
th	Thermal
TSA	Temperature swing adsorption
WH	Wall-heated
XRD	X-ray diffraction
α-Fe_2O_3	Hematite
γ-Fe_2O_3	Maghemite

(continued on next column)

(continued)

Nomenclature	**Description**	**Unit**
A	Specific surface area	m^2/g
B	Magnetic field strength	mT
c_p	Mass specific heat capacity	$J/g\,K$
d	Diameter	mm
E	Energy	MJ/kg
f	Frequency	kHz
H_c	Coercivity	Oe
ΔH_{Ads}	Heat of adsorption	kJ/mol
HR	Heating rate	$^{\circ}C/min$
I	Electric current	A
K_c	proportional gain	$A/^{\circ}C$

(continued on next page)

* Corresponding author.
E-mail address: javier.fernandez@iqs.url.edu (J. Fernandez-Garcia).

https://doi.org/10.1016/j.cej.2026.174901
Received 11 December 2025; Received in revised form 10 February 2026; Accepted 3 March 2026
Available online 4 March 2026

(*continued*)

L	Length	m
$\widetilde{M}$	Molar mass	g/mol
M_r	Remanent magnetization	emu/g
M_s	Saturation magnetization	emu/g
m	Mass	g
$\dot{m}$	Mass flow	mg/s
N	Number of coil turns	–
$\dot{n}$	Molar flow	mol/s
n	Molar amount	mol
P	Electric power	W
p	Pressure	kPa
productivity	Productivity	$mg/g\,s$
purity	Purity	%
Δq	Effective working capacity	$mmol/g$
$\overline{\Delta q}$	Mean effective working capacity	$mmol/g$
R	Radius	m
recovery	Recovery	%
SAR	Specific absorption rate	W/g_{MAC}
t	Time	s
T	Temperature	$^{\circ}C$
V	Specific pore volume	cm^3/g
x	Mass fraction	%
y	Volume fraction	%
δ	Electromagnetic skin depth	mm
ε	Relative error	%
η	Energy efficiency	%
μ_0	Permeability of free space	H/m
μ_r	Relative permeability	–
σ_{el}	Electric conductivity	$1/\Omega\,cm$
σ_q	Standard deviation of mean working capacity	$mmol/g$
τ_d	derivative time	s
τ_i	integral time	s

Keywords

Magnetic adsorption composite
Induction heating
Temperature feedback loop control
Process intensification
Electrified carbon capture
TSA

1. Introduction

Anthropogenic CO_2 emissions are the main driver of climate change [1] and intensify global warming since the industrial revolution [2]. As a key component of climate mitigation strategies, carbon capture has gained increasing attention in recent years [3]. Post combustion carbon capture (PCCC) technologies are essential for reducing CO_2 emissions from point sources such as industrial flue gases [4,5], which typically can contain $3-33$ *vol*% CO_2 [6,7]. Adsorption processes have the potential to reduce costs together with environmental footprint, compared to amine-based solvents [8]. Among these, temperature swing adsorption (TSA) has been widely explored due to its simplicity and scalability while allowing for very high purity CO_2 (99%) at high recovery (95%) [9,10]. TSA is a cyclic adsorption process that exploits the temperature-dependent adsorption-desorption properties of adsorbents to capture and separate CO_2 from gas mixtures [11]. The heat generation of conventional TSA lays on the outside of the reactor, heating the bed either indirectly by thermal conduction through the reactor walls or directly by using a hot gas from the column inlet [12,13]. Common CO_2 adsorbent materials used in TSA include zeolites (zeolite 5A [14], zeolite 13X [15], etc.), carbon molecular sieves (CMS) [16], silica [17] or metal organic frameworks (MOFs) (Mg-MOF-74 [18], HKust-1 [19], etc.) all of which exhibit high CO_2 capacity and selectivity [10]. The low heat transfer of these adsorbent materials [20,21] leads to slow heating rates and the formation of thermal gradients within the adsorbent bed, thereby reducing the overall process efficiency [22,23]. Furthermore, traditional TSA systems depend on thermal energy sources, such as steam or combustion [24]. Electrifying TSA through induction heating is a promising pathway to overcome the thermal limitations of conventionally heated TSA while allowing for a sustainable and flexible operation, particularly when coupled with renewable electricity sources [25].

Induction heating, following Ampère's law, is based on running an oscillating electric current through an induction coil to produce an approximately oscillating homogeneous magnetic field inside of it [26]. To enable induction heating, the adsorbent material inside of the induction coil must be susceptible to those oscillating magnetic fields [27]. Since conventional CO_2 adsorbents intrinsically lack responsiveness to electromagnetic fields [28], additives are needed to complement the adsorbent's properties. The heat releasing mechanisms of induction heating are hysteresis loss, Néel relaxation and Eddy current dissipation [29]. While Eddy currents would not require magnetic properties, but a high electrical conductivity, induction heated TSA commonly relies on the incorporation of magnetic particles. Typically, maghemite (γ-Fe_2O_3) [30], magnetite (Fe_3O_4) [19], and magnesium ferrite ($MgFe_2O_4$) [18] are used as magnetic heating components due to their favorable magnetic properties such as high saturation magnetization [31]. Fe_3O_4 can be oxidized by thermal treatment from 200 °C to 250 $^{\circ}C$ in dry conditions and even at lower temperatures when moisture is present [32]. The integration of such particles into CO_2 adsorbents results in magnetic adsorption composites (MACs), which simultaneously possess high CO_2 adsorption capacity and magnetic susceptibility. With the thermal source laying inside the adsorbent bed, induction heating can provide rapid and targeted heating of the adsorbent with heating rates higher than 100 $\frac{^{\circ}C}{min}$ [33,34], while conventional TSA heating rates of the adsorption bed are reported to be lower than 20 $\frac{^{\circ}C}{min}$ [23,35]. Much of the literature on MAC focuses on the intrinsic properties, adsorption capacity and magnetic susceptibility [28,34,36], but less attention has been given to the structural design of MACs for PCCC induction heating TSA and to their performance under adsorption-desorption cycles.

The most common and easy method to synthesize a MAC from two powder precursors is to first mix the dry powders and then create the homogeneous MAC particle. Since mass transfer in and out of CO_2 adsorbent structures are diffusion driven [37,38], a core-shell design can be an alternative MAC design, to expose the outer shell made of adsorbent to the gas environment and the magnetic material, that does not require gas contact, as a heating core. A side effect of that structure can be the steeper temperature gradient from the inside of the MAC to its surface, due to the low thermal conductivity of the adsorbent shell. At high temperatures, gas diffusion in the pores is accelerated [25,30]. The CO_2 adsorbed closer to the center of the particle should experience higher temperatures and should desorb more quickly. Alternatively, instead of integrating magnetic and adsorptive properties within a single particle, separate heating and adsorbing particles can be packed together in the adsorption bed. This approach is particularly suitable when existing adsorbent particles are to be used or when processing challenges with dual-function materials (MACs) arise.

For the inductively heated desorption step, a temperature feedback control is desired not only for safe operation but also to allow for process intensification: Lin et al. reported a reduction in desorption time from 128 *s* to 86 *s* and an enhanced energy efficiency from 68.4% to 79.2% when switching from constant energy input to temperature feedback control [39]. Homogeneous pellets of Fe_3O_4/zeolite 13× were reported to exhibit a high desorption rate of 1.72 $\frac{mgCO_2}{g_{MAC}\cdot s}$ (regenerating the adsorbent by 95%) under a magnetic field strength of 22.8 mT. A combined evaluation of a MAC's productivity and regeneration energy was done for homogeneous $MgFe_2O_4$/Mg-MOF-74 [18] and Fe_3O_4/HKust-1 [19] composites with 0.68 $\frac{mgCO_2}{g_{MAC}\cdot s}$ for 2.77 $\frac{kJ}{gCO_2}$ and 0.38 $\frac{mgCO_2}{g_{MAC}\cdot s}$ for 4.4 $\frac{kJ}{gCO_2}$, respectively.

Building on the current trend in the literature that focuses primarily on the intrinsic material properties of MACs, we take the next step by

investigating how different material design strategies perform in a complete induction-heated TSA process. Zeolite 13× and Fe_3O_4 were selected as low-cost and widely available adsorbent and heating components. Our goal is to evaluate both the potential and the practical limitations of each design when fast, induction-based heating is controlled via a temperature feedback loop.

Beyond adsorption performance, the materials are evaluated by linking their magnetic heating behavior to CO_2 capture over multiple adsorption-desorption cycles and by analyzing the associated energy efficiency from electrical grid input to thermal energy generation and ultimately to CO_2 desorption. This system-level perspective enables a direct comparison between induction heating and resistive wall heating and provides guidance for future materials development and experimental scale-up.

2. Experimental section

The four MAC structure designs studied are shown in Fig. 1: a) Homogeneously mixed (HG) zeolite 13× with Fe_3O_4, b) core-shell (CS) design with a Fe_3O_4 heating bead as core and a zeolite 13× shell around, c) mixed bed (MB) of Fe_3O_4 heating beads and zeolite 13× beads, and d) only zeolite 13× beads as comparison, that are either resistively heated over the column wall (WH) or tested for room temperature (RT) desorption with purge gas only. The MB was created by mixing adsorbent and heating beads in the desired mass ratio and filling the adsorption bed such that the heating beads are well distributed among the adsorbent beads. In the following, MB will be considered a MAC as the bed as a whole exhibits magnetic and adsorption properties. The schematic of each adsorbent is shown in Fig. 1.

2.1. Materials

Zeolite 13× ($Na_{86}[(AlO_2)_{86}(SiO_2)_{106}]$ x H_2O powder, 2.72 μm), Fe_3O_4 (powder, $< 5\ \mu m$, 95%), α-Fe_2O_3 (hematite, powder, $< 5\ \mu m$, 96%), carboxymethyl cellulose (CMC, powder, high viscosity), bentonite (nanoclay, hydrophilic bentonite) and SiO_2 (50–70 mesh particle size) were purchased from Sigma-Aldrich (Spain). CO_2 (99.5%) and N_2 (99.998%) are supplied by Carburos Metálicos (Spain).

2.2. Magnetic adsorbent composite production

To evaluate how material design affects the induction-based TSA performance, MACs were prepared with identical overall composition and bead size, but different particle structure design. Preliminary heating tests indicated that Fe_3O_4 powder exhibited the optimal induction heating performance after 3h of thermal treatment at 250°C in air (see Fig. S1 Supplementary Material (SM)).

The composite formulation was based on Gholami et al., 2022 [25], with modifications to the binder system. Bentonite was used as the binder for the Fe_3O_4, although it was not suitable for forming a shell structure for CS. In contrast, CMC was suitable to create a shell at 5% binder content; however, with low thermal stability above 200°C [40].

The powders were thoroughly mixed in a beaker, and deionized water $\left(\approx 0.7\ \frac{g_{H_2O}}{g_{dry\ powders}}\right)$ was added gradually until a viscous paste was formed. This paste was then hand-shaped into spherical beads. In this process, the synthesis of CS beads was size limiting due to the shell formation step. CS beads of $d_1 \approx 1.7\ mm$ and $d_2 \approx 4.1\ mm$ diameter could be well reproduced. HG beads, zeolite 13× adsorbent beads and Fe_3O_4 heating beads were then synthesized to match the dimensions and composition of CS.

After shaping the respective beads, Fe_3O_4 containing beads were heat-treated at 250°C in air, whereas CMC-containing beads were dried at 180°C. This temperature was chosen to not further influence the oxidation of Fe_3O_4, thus remain comparable with HG, and not damaging the CMC binder. In the case of CS production, firstly the heating bead was produced, thermally treated and subsequently surrounded by adsorbent shell.

Table 1 summarizes the dried MAC composition, thermal treatment conditions, tested sample mass, and resulting bead radius.

Table 1
Thermal treatment of sample production and composition of dry MAC in mass fractions. Furthermore, the total sample mass filled in the adsorption column and the bead diameter are given.

	HG	CS	MB	WH & RT
Thermal treatment	3h at 250°C	Heating bead: 3h at 250°C After adding shell: 3h at 180°C	Heating bead: 3h at 250°C Adsorbent bead: 3h at 180°C	3h at 180°C
$x_{zeolite\ 13X}/(\%mass)$	78.9	77.4	75.7	94.8
$x_{Fe_3O_4}/(\%mass)$	16.3	17.6	19.4	0.0
$x_{CMC}/(\%mass)$	0.0	4.1	3.9	5.2
$x_{bentonite}/(\%mass)$	4.8	0.9	1.0	0.0
$m_{MAC}/(g)$	0.56	0.55	0.75	0.62
$d_1/(mm)$		Heating bead: 1.68 ± 0.04	Heating bead: 1.60 ± 0.12	
$d_2/(mm)$	3.82 ± 0.10	Adsorbent bead: 4.14 ± 0.16	Adsorbent bead: 4.26 ± 0.14	3.61 ± 0.22

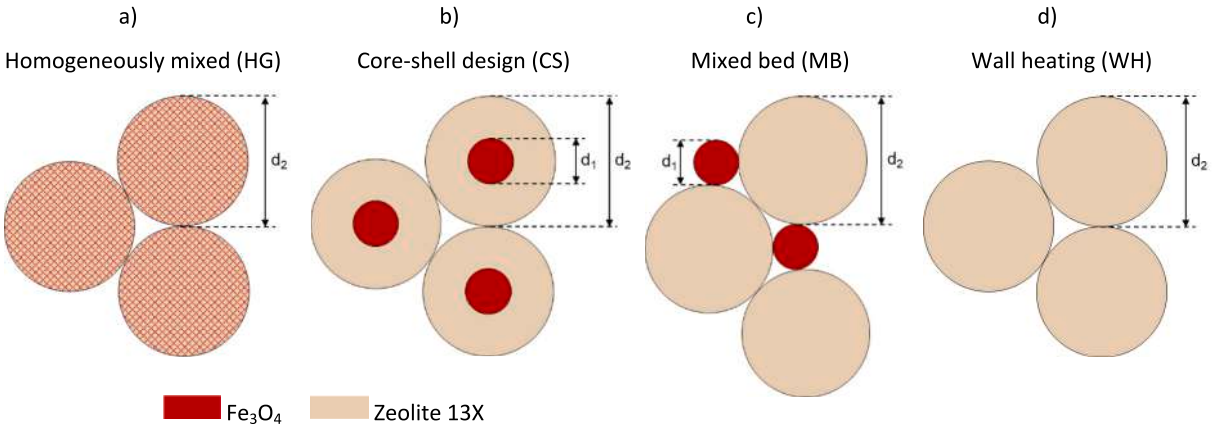

Fig. 1. Cross-sectional schematic structure of magnetic adsorption composites (MACs) in the adsorption bed with indication of bead diameters d_1 and d_2.

2.3. Material characterization

The magnetic properties of the synthesized adsorbents were characterized using a Superconducting Quantum Interference Device - Vibrating Sample magnetometer (SQUID-VSM), model MPMS3 from Quantum Design with he vibrating frequency 16.5 *Hz*, and the samples were measured with a vibrating amplitude of 0.5 *mm* and the measurement averaging time per data point was 2 seconds, stabilizing the field at each point.

The MAC beads were grinded down and in the case of CS and MB thoroughly homogenized. 30 to 40 *mg* of dried sample were loaded into the holder and subjected to an applied magnetic field strength (B $[mT]$) ranging from -30000 to $+30000$ *Oe*.

The crystalline phases of synthesized MAC samples and the pristine materials were characterized by X-ray diffraction (XRD) in a Bragg-Brentano geometry using Cu-Kα radiation, coupled with a PIXcel Medipix 3 detector (Empyrean, Malvern Panalytical).

The specific surface area and pore volume were determined measuring the N_2 physisorption at 77 *K* using a high vacuum adsorption analyzer (Autosorb 6200, Anton Paar). Therefore, the MAC beads were grinded down, in the case of CS and MB thoroughly homogenized, and around 100 *mg* of adsorbent used for measurement. The Brunauer-Emmett-Teller (BET) method was applied to calculate the specific surface area from the linear portion of the adsorption isotherm at relative pressures ($\frac{p}{p_0}$) between 0.05 and 0.30. The pore volume was calculated by t-plot method.

The Specific Absorption Rate (SAR $\left[\frac{W}{g_{MAC}}\right]$) was measured at magnetic field strengths up to 35.6 *mT*, corresponding to the maximum field achievable with the induction heating unit and the coil used in this study. The *SAR* of CS and MB was determined based on the *SAR* of the heating bead, which acts as the heating source in each MAC design, and scaled according to their mass fraction in the MAC adsorption bed (Table 1). To obtain reliable *SAR* measurements, the heating material is commonly combined with a thermal buffer additive of known heat capacity. Since the rotational freedom of magnetic particles influences *SAR* [41], measurements were performed using two different thermal buffer additives. Firstly, the *SAR* of the heating materials dispersed in water was measured, as this is a common method to compare the magnetic induction heating performance of a material [25]. Secondly, the *SAR* of the heating materials in the immobilized, dry state was measured to represent the induction TSA heating conditions.

For these measurements, the HG and heating beads were grinded to a powder using a mortar. To measure the *SAR*, a small mass of the respective powder was placed in an insulated borosilicate glass tube together with the heating buffer additive and the FISO-FPI-HR fiber optic temperature sensor. It was ensured that the sensor was fully submerged in the suspension or powder, respectively. In case of HG, the powder inherently contained zeolite 13×, while for the immobilized *SAR* measurement of the heating bead SiO_2 powder was used as a thermal buffer additive in order to match the $x_{Fe_3O_4} \approx 20\%$ as it is present in HG. The exact masses used in the *SAR* measurement experiments can be found in Table S1 in the SM. The insulated sample tube containing MAC, thermal buffer additive and temperature sensor were then placed inside the heating coil to measure the temperature kinetic curve $T(t)$ under a certain magnetic field strength. The respective *SAR* calculates then as given in eq. (1):

$$SAR(B) = \sum_i x_i \, c_{p,i} \, \frac{\Delta T}{\Delta t} \tag{1}$$

With x_i [%] being the mass fraction and $c_{p,i}$ $\left[\frac{J}{g\,K}\right]$ the mass specific heat capacity of each material heated by the inductive heating setup, including the MAC components, thermal buffer additives, and the effectively heated part of the glass tube. The $c_{p,i}$ values of the MAC components, as well as that of the thermal buffer additives and the sample tube, were sourced from published literature values and can be found in Table S2 in the SM. Finally, the immobilized *SAR* was then fitted by logistic fit) [42] to calculate the energy spent during temperature feedback loop controlled desorption.

2.4. Experimental setup

The experimental setup used in this work is shown in Fig. 2. The adsorption column consisted of a temperature resistant Duran glass column (10 *mm* outer diameter, 1 *mm* wall thickness) supplied by Vidrasa (Spain). Glass beads of 1 *mm* were used to support the adsorbent bed, to avoid run-in effects and to reduce the dead volume in the adsorption column. The CO_2 and N_2 feed flow was controlled by mass flow controllers (El-Flow FC-101 and FC-102, Bronkhorst (Netherlands)). The CO_2 outlet concentration was monitored continuously with an infrared gas sensor (Linearity error $< 0.9\%$, Flow Evo F3–212108-05000, smartGAS Mikrosensorik GmbH (Germany)) coupled with the corresponding data acquisition software (1 *s* sampling rate, smartGAS Data Logger, smartGAS Mikrosensorik GmbH (Germany)). An induction heating unit (1 *kW* EASYHEAT, Ambrel (United Kingdom)l) supplied an alternating magnetic field by running an alternating current (AC) through a water-cooled copper coil (3 *cm* internal diameter, 4 *cm* effective length, 5 turns), around the adsorption column. The AC frequency provided by the induction heating unit depends on the applied electric current itself. In the effective AC range used in the desorption experiments, from 100 *A* to the maximum of 283.3 *A*, the frequency was between 273 *kHz* and 257 *kHz*. The characterization of electric current (I° $[A]$), frequency (f° $[kHz]$) and electric power usage of the induction heating unit is shown in Fig. S2 in the SM. The temperature inside of the reactor was measured by a fiber optic temperature sensor (Sensor: FOT-L-SD-C1-F1-M2-R1-ST, FISO; Signal conditioner: FTI-10, Fiso (Canada)) placed inside the adsorbent bed. Both the induction unit and the fiber optic temperature sensor were connected to a LabVIEW program (LabVIEW Full Development System Version: 2023 Q1, National Instruments (USA)). A temperature feedback loop with proportional-integral-derivative (PID) controller through LabVIEW was used to reach a temperature setpoint by controlling the electric current through the coil. The system was controlled using a parallel-form proportional-integral-derivative (PID) controller. The tuning of the controller parameters proportional gain (K_c $[A/^{\circ}C]$), integral time (τ_i $[s]$), and derivative time (τ_d $[s]$) aimed to achieve fast heating with limited overshoot and no sustained oscillations. Structured tuning methods such as Ziegler-Nichols or internal-model control were considered, however their application requires reliable determination of the process gain under steady-state conditions at the relevant operating currents. In the present system, steady-state temperature measurements at amperages above 200 *A* were not feasible due potential material alteration and temperature-sensor limitations. Moreover, *SAR* measurements have a non-linear dependence of heat generation on magnetic field strength [42], making extrapolation from lower-field measurements unreliable. Consequently, the controller parameters were manually tuned by iteratively adjusting their values and observing the system's response. The final tuned values were: $K_c = 3.00$, $\tau_i = 1.25\ s$, $\tau_d = 0.10\ s$.

To represent WH, external heating was investigated using a direct current (DC) power supply (SPS-3010 N, Jesverty (China)) and resistance wire (Constantan, 27 *AWG*, 2.44 Ω/m, 4 strands of 20 *cm* length, SourcingMap (China)) wound around the section of the adsorption column containing the adsorbent bed.

2.5. Adsorption - desorption cycle

The adsorption column was filled with MAC such that the adsorption bed is fully covered by the coil (Adsorption bed height: $3.5 - 4.0$ *cm*) and the fiber optic sensor placed accordingly within the MAC bed. The

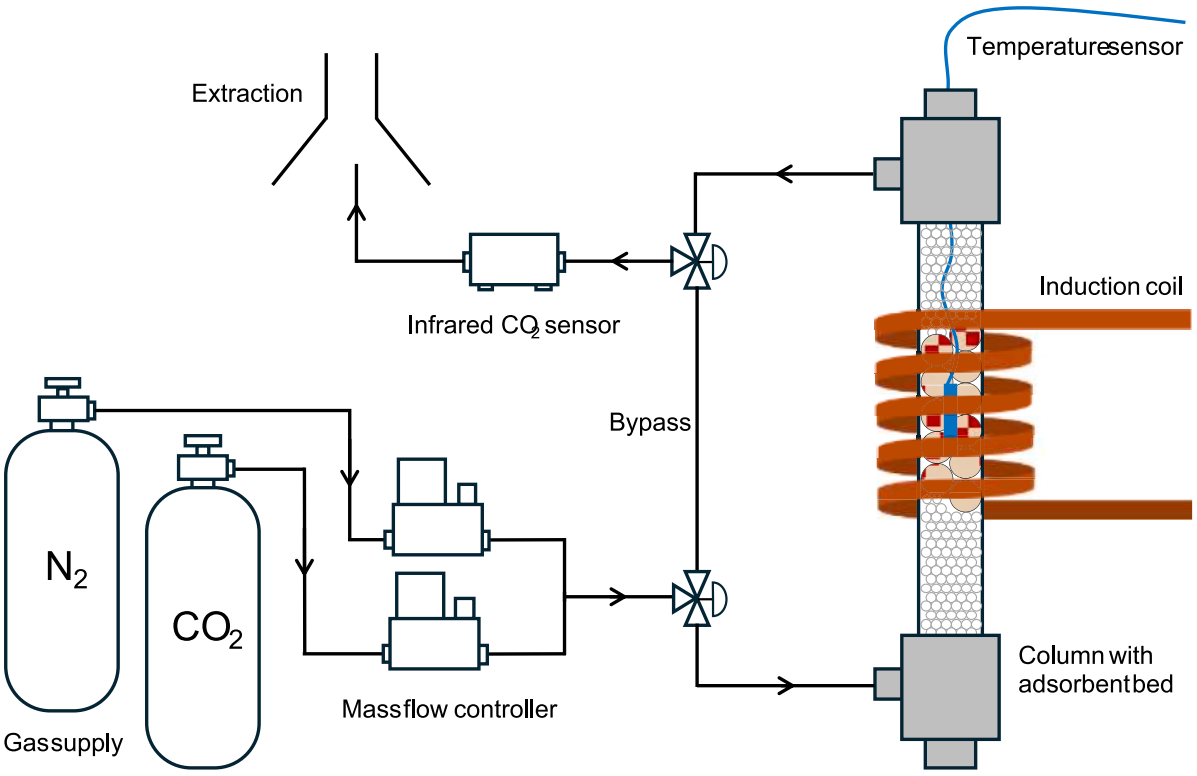

Fig. 2. Schematic experimental setup for CO_2 adsorption-desorption cycles.

resulting mass of the adsorbent bed is given as m_{MAC} in Table 1. To remove the majority of adsorbed moisture, the adsorbent bed was heated to 120 $^{\circ}C$ using the respective electric heating method under a N_2 flow of 50 Nml/min for 60 min. Adsorption experiments were conducted at ambient pressure under an inlet N_2 and CO_2 flow of 20.0 $\frac{Nml}{min}$ and 3.5 $\frac{Nml}{min}$ respectively, corresponding to a $y_{CO_2,in} = 15\% v/v$ CO_2 in N_2 mixture. The outlet CO_2 concentration y_{CO_2} was measured over time by the infrared CO_2 sensor. Desorption experiments were carried out at ambient pressure by adjusting the inlet gas flow to 20 $\frac{Nml}{min}$ of N_2 and simultaneously starting the heating process with the desired temperature setpoint. After no more CO_2 was measured in the outlet, the adsorption column was cooled down to ambient temperature under a 20 $\frac{Nml}{min}$ N_2 flow through the adsorption bed. To adjust $y_{CO_2,in}$, the gas flow was first directed through the bypass and then back to the adsorption column to start adsorption or desorption, after the system setup has developed the new condition.

The LabVIEW program tracked the electric current, the reactor temperature over time and simultaneously y_{CO_2} by the infrared CO_2 sensor. WH experiments were carried out to represent conventional TSA heating over the column wall. For WH, an additional measurement was carried out in which the temperature sensor was placed between the heating wire and the reactor wall to record the external temperature response at a given electrical power. RT desorption was tested to evaluate the influence of N_2 flow on the desorption process at room temperature.

The time after which adsorption $t_{end,ads}$ and desorption $t_{end,des}$ experiments were considered complete was when y_{CO_2} reached the inlet concentration $y_{CO_2,0}$ of each respective step ($y_{CO_2} = 0.15$ for adsorption and $y_{CO_2} = 0$ for desorption). Considering a constant N_2 flow ($\dot{n}_{N_2}$ $\left[\frac{mol}{s}\right]$), the outlet CO_2 stream ($\dot{n}_{CO_2}$ $\left[\frac{mol}{s}\right]$)was calculated from measured y_{CO_2} as in eq. (2):

$$\dot{n}_{CO_2}(t) = \frac{y_{CO_2}(t)}{1 - y_{CO_2}(t)} \bullet \dot{n}_{N_2} \tag{2}$$

The amounts of adsorbed CO_2 ($n_{CO_2,ads}$ $[mol]$) and desorbed CO_2 ($n_{CO_2,des}$ $[mol]$) were calculated by integrating the outlet CO_2 stream as in eqs. (3) and (4):

$$n_{CO_2,ads} = \dot{n}_{CO_2,ads,in} \bullet t_{end,ads} - \int_0^{t_{end,ads}} \dot{n}_{CO_2}(t)dt \tag{3}$$

$$n_{CO_2,des} = \int_0^{t_{end,des}} \dot{n}_{CO_2}(t)dt \tag{4}$$

The inlet CO_2 flow rate during adsorption ($\dot{n}_{CO_2,ads,in}$ $\left[\frac{mol}{s}\right]$) was determined from the inlet CO_2 volume fraction $y_{CO_2,in}$ using Eq. (2), measured when running the inlet flow through the bypass. Adsorption-desorption cycles were repeated until a steady state of 5 cycles was reached.

When adsorption and desorption are in steady state, the measured adsorption amount equals the desorbed amount of the previous cycle. Hence, the effective working capacity (Δq_{CO_2} $\left[\frac{mmol}{g_{MAC}}\right]$) was determined under steady-state conditions as the ratio of the adsorbed CO_2 amount ($n_{CO_2,ads}$ $[mol]$) to the mass of the MAC (m_{MAC} $[g]$). The relative error (ε [%]) of the steady-state effective working capacity was estimated as the ratio of the standard deviation (σ_q $\left[\frac{mmol}{g_{MAC}}\right]$) to the mean effective working capacity ($\overline{\Delta q}_{CO_2}$ $\left[\frac{mmol}{g_{MAC}}\right]$).

$$\varepsilon = \frac{\sigma_q}{\overline{\Delta q}_{CO_2}} \bullet 100\% \tag{5}$$

The magnetic field strength applied by the induction coil was

estimated from the dimensions of the induction coil and I [43]:

$$B = \frac{\mu_0 \bullet N \bullet I}{2\sqrt{R^2 + (L/2)^2}} \bullet 10^{-3} \quad (6)$$

With $\mu_0 = 4\pi \bullet 10^{-7}\frac{H}{m}$ being the permeability of free space [44], R [m] the radius, L [m] the length and N [−] the number of turns of the coil.

In this study, the effective operating frequency ranged between 273 kHz and 257 kHz as shown in Fig. S2. The field-dependent heating performance, expressed as $SAR(B)$ was measured for all heating materials over the range of applied I by the induction heating unit up to 283.3 A, corresponding to magnetic field strengths up to 35.6 mT (Eq. (6)). $SAR(B)$ was fitted by logistic fit (Eq. S1).

During the desorption step, the magnetic field strength varied over time due to the temperature feedback control of the induction heating unit, and with it the thermal energy release at every moment. Although desorption was continued until no CO_2 was detected in the effluent gas, the heating process was defined in post-processing as complete when 99% of the total measured CO_2 amount had been desorbed ($t_{end,heating}$ [s]). To determine the total released heating energy of the MAC during induction heating ($E_{heating,IH}$ $\left[\frac{MJ}{kg_{MAC}}\right]$), $SAR(B(t))$ was integrated at each time step until $t_{end,heating}$.

$$E_{heating,IH} = \int_0^{t_{end,heating}} SAR(B(t))dt \bullet 10^{-3} \quad (7)$$

In the case of WH, the applied electric power (P_{WH} [W]) was given by the DC power supply and held constant throughout the desorption process. Assuming that all of the electric energy dissipated to heat, this P_{WH} was used to calculate $E_{heating,WH}$ for resistive wall heating.

$$E_{heating,WH} = \frac{P_{WH} \bullet t_{end,heating} \bullet 10^{-3}}{m_{ads}} \quad (8)$$

Besides comparing of heat released in the different TSA heating methods, the process energy efficiency was evaluated in respect to the amount CO_2 desorbed. For IH, the specific electrical energy input from the grid per mass of desorbed CO_2 ($E_{grid,IH}$ $\left[\frac{MJ}{kg_{CO_2}}\right]$) was calculated from the time integral of the electric power ($P_{IH}(t)$ [W]) recorded by the induction heating unit, divided by the desorbed CO_2 mass.

$$E_{grid,IH} = \frac{\int_0^{t_{end,heating}} P_{IH}(t)dt}{\Delta q_{CO_2} \bullet \widetilde{M}_{CO_2} \bullet m_{MAC}} \quad (9)$$

The corresponding thermal energy released during induction heating in respect to the desorbed CO_2 mass was calculated as by Eq. (10).

$$E_{th,IH} = \frac{E_{heating,IH}}{\Delta q_{CO_2} \bullet \widetilde{M}_{CO_2}} \quad (10)$$

For resistive wall heating, electrical losses were assumed negligible such that the electrical grid energy of WH experiments equals the thermal energy released:

$$E_{grid,WH} = E_{th,WH} = \frac{E_{heating,WH}}{\Delta q_{CO_2} \bullet \widetilde{M}_{CO_2}} \quad (11)$$

Independent of the heating method, the minimum regeneration energy ($E_{reg,min}$ $\left[\frac{MJ}{kg_{CO_2}}\right]$) required in CO_2 TSA is described by the heating of the MAC and the energy of the endothermic desorption process (12)) [18,19,36,39].

$$E_{reg,min} = \frac{m_{MAC}\left(c_{p,MAC}\left(T_{des} - T_{ads}\right) - \Delta H_{Ads}\,\Delta q_{CO_2}\right)}{n_{CO_2,des} \bullet \widetilde{M}_{CO_2}} \bullet 10^{-3} \quad (12)$$

With c_p $\left[\frac{J}{g\,K}\right]$ being the mass specific heat capacity of the MAC and $\Delta H_{Ads} = -34.9$ $\left[\frac{kJ}{mol}\right]$ the heat of adsorption of CO_2 on zeolite 13× [45]. As $E_{reg,min}$ represents a theoretical minimum, it enables comparison of different MACs independent of the experimental setup.

Electrical ($E_{loss,el}$ $\left[\frac{MJ}{kg_{CO_2}}\right]$) and thermal ($E_{loss,th}$ $\left[\frac{MJ}{kg_{CO_2}}\right]$) losses were then defined as:

$$E_{loss,el} = E_{grid} - E_{th} \quad (13)$$

$$E_{loss,th} = E_{th} - E_{reg,min} \quad (14)$$

Finally, the electrical efficiency (η_{el} [%], from grid to heat), thermal efficiency (η_{th} [%] and from heat to CO_2 desorption) were calculated as:

$$\eta_{el} = \frac{E_{reg,min}}{E_{grid}} \quad (15)$$

$$\eta_{th} = \frac{E_{reg,min}}{E_{th}} \quad (16)$$

It should be noted that the use of a purge gas contributes to the desorption process, but it is not accounted for in the calculations of the energy used. This effect will be considered in the evaluation of MAC performance through the recovery [%], purity [%] and productivity $\left[\frac{mg_{CO_2}}{g_{MAC} \cdot s}\right]$ of the desorption process.

The purity of the desorbed product gas was calculated according to Eq. (17) and the recovery according to Eq. (18) [46]. During desorption, a typical profile of $\dot{n}_{CO_2}(t)$ shows an initial CO_2 peak that gradually tails off [30], while $\dot{n}_{N_2}$ remains constant. Consequently, the calculated purity can be influenced by the chosen criterion for the end of desorption ($t_{end,des}$ [s]). Selecting a shorter $t_{end,des}$ increases the product purity but reduces the recovery in a single adsorption-desorption cycle, or, when multiple cycles are performed, reduces the effective working capacity at steady-state.

$$\text{purity} = \frac{\int_0^{t_{end,des}} \dot{n}_{CO_2,des}(t)dt}{\int_0^{t_{end,des}} \dot{n}_{CO_2,des}(t)dt + \dot{n}_{N_2} \bullet t_{end,des}} \quad (17)$$

$$\text{recovery} = \frac{\int_0^{t_{end,des}} \dot{n}_{CO_2,des}(t)dt}{\dot{n}_{CO_2,ads,in} \bullet t_{end,ads}} \quad (18)$$

In this work the focus was placed on the effective working capacity at steady-state, obtained at full saturation of the adsorbent bed during adsorption and after complete desorption at a certain desorption temperature. Therefore, recovery and purity were not explicitly calculated. However, the potential trade-off between purity and recovery (or the effective working capacity) is discussed qualitatively based on the desorption curves of the investigated materials at different desorption temperatures.

The productivity is a quantitative indicator that combines effects of the working capacity and heating performance of a MAC (Eq. (19)) [19] and will be discussed in this work. It should be emphasized that the productivity here only refers to the desorption step, as adsorption time and cooling down and are influenced by the design of the adsorption

column and also by the material design of the MAC.

$$\text{productivity} = \frac{\int_0^{t_{end}} \dot{n}_{CO_2,des}(t) \bullet \widetilde{M}_{CO_2} dt \bullet 10^{-3}}{m_{MAC} \bullet t_{end,des}} \quad (19)$$

3. Results and discussion

3.1. Material characterization

The synthesized MACs are shown in Fig. 3. The brownish coloration of samples indicates partial oxidation of the Fe_3O_4 powder [32] whereas the white color correspond to the zeolite 13× structure. HG sample exhibited a homogeneous but lighter red color compared to the magnetic cores in CS and MB. The core of the CS can be seen to be in close contact with the surrounding shell.

The influence of the synthesis procedure on the zeolite structure and oxidation of the Fe_3O_4 heating bead used in CS and MB was assessed by XRD measurements (see Fig. 4). For this, the synthesized HG and the heating beads were measured together with pristine zeolite 13×, Fe_3O_4 and α-Fe_2O_3. The XRD patterns of Fe_3O_4, γ-Fe_2O_3 and α-Fe_2O_3 were taken from Cornell et al. (2003) [32].

Fe_3O_4 and γ-Fe_2O_3 have similar XRD peaks. The oxidation of Fe_3O_4 to γ-Fe_2O_3 in the heating bead can be confirmed by comparison with the pristine Fe_3O_4. Indicators are the reduced peak of Fe_3O_4 at 18.2° and 37.1° as well as by the extending the Fe_3O_4 peaks at 56.9° and 62.5° to double peaks at 57.4° and 63.0°, respectively. A low oxidation in the heating bead to α-Fe_2O_3 is present, as can be seen by the characteristic peak at 33.2°. As expected, HG shows a combination of the zeolite 13× and Fe_3O_4/γ-Fe_2O_3 peaks. Due to overlapping with the zeolite 13× pattern, it cannot be clarified whether oxidation from Fe_3O_4 to γ-Fe_2O_3 or even to α-Fe_2O_3 took place, compared to the heating bead. Comparing HG with pristine zeolite 13× powder, the crystal structure of zeolite 13× remained unchanged by the 250°C thermal treatment.

To assess both the textural and magnetic properties of the MAC, nitrogen physisorption (BET) and superconducting quantum interference device (SQUID) were conducted. BET measurements provided insights into the specific surface area (A_{BET} $\left[\frac{m^2}{g_{MAC}}\right]$) and pore volume ($V_{pore}$ $\left[\frac{cm^3}{g_{MAC}}\right]$) of the zeolite 13× in the MAC. SQUID analysis was used to evaluate the magnetic behavior of the F_3O_4 phase under applied magnetic fields, which is critical for the material's potential in induction heating applications. From SQUID analysis, the magnetic saturation magnetization (M_s $\left[\frac{emu}{g_{MAC}}\right]$), remanent magnetization (M_r $\left[\frac{emu}{g_{MAC}}\right]$) and coercivity ($H_c$ [Oe]) were determined. The N_2 physisorption and SQUID measurements are given in the SM in Fig. S3 and Fig. S4, respectively, and the magnetic and structural properties obtained from both are summarized in Table 2.

The surface areas of the synthesized MACs are reduced to approximately 54%to 59% of that of pristine zeolite 13×, while the zeolite 13X content of the composites ranges from 75%to 79% (as shown in Table 1). The N_2 physisorption isotherms of pristine zeolite 13× and the three MACs (HG, CS and MB) are shown in Fig. S3 in the SM. All samples exhibit characteristic Type I isotherms [47], confirming that the microporous structure of zeolite 13× is preserved after composite synthesis. No pronounced hysteresis loop is observed for any sample, indicating the absence of significant mesoporosity. Therefore, the discrepancy between the MAC surface area and pristine zeolite 13× likely arises from binder coverage and pore accessibility limitations rather than structural degradation of the zeolite framework. The slightly higher surface area and pore volume of HG, despite its marginally lower zeolite 13× content, are attributed to the use of bentonite as a binder, whereas CS and MB were prepared using CMC. At relative pressures approaching saturation, MB composite shows an additional uptake compared to HG, CS and pristine zeolite 13×. While the exact origin of that behavior cannot be directly explained by the synthesis protocol, it can be attributed to adsorption in interparticle voids arising from the mixed-bed configuration and the coexistence of different particle size fractions.

As previously mentioned, the color changes in samples and XRD findings suggest the oxidation of Fe_3O_4 mainly to γ-Fe_2O_3 but only a small fraction to α-Fe_2O_3, which forms subsequently from γ-Fe_2O_3 [32]. VSM measurements showed ferrimagnetic behavior of the three MACs, typical for Fe_3O_4 and γ-Fe_2O_3, while α-Fe_2O_3 is known to be weakly ferromagnetic [32]. HG exhibited lower magnetic properties compared to CS and MB, indicating differences in the dominant iron oxide phase.

The literature M_s values of Fe_3O_4 and γ-Fe_2O_3 and α-Fe_2O_3 at ambient conditions are $M_{s,Fe_3O_4} = 92 - 100\ \frac{emu}{g_{MAC}}$, $M_{s,\gamma-Fe_2O_3} = 60 - 80\ \frac{emu}{g_{MAC}}$ and $M_{s,\alpha-Fe_2O_3} \approx 0.3\ \frac{emu}{g_{MAC}}$, respectively [32]. Considering the iron oxide content of $x_{Fe_3O_4} \approx 20\%$ in the MAC samples, the magnetic properties of CS and MB correspond to those of Fe_3O_4 while HG aligns more closely with γ-Fe_2O_3. This suggests that oxidation in HG formed more α-Fe_2O_3 than in the CS and MB.

Following the structural and magnetic characterization, the induction heating performance of the different MACs was evaluated under varying magnetic field strength. Fig. 5 shows the *SAR* of the studied materials as a function of magnetic field strengths up to 35.6 *mT*. The *SAR* behavior with *B* was fitted by logistic fit (Eq. S1) [42] to calculate the energy released depending on the magnetic field strength by the induction heating unit. The fitting parameters can be found in the SM under Table S3.

As expected from the VSM results (Table 2), the heating efficiency correlates with the magnetic properties of the heating material. The higher heating performance of the CS and MB heating beads compared to HG is therefore attributed to their superior magnetic characteristics. These differences likely arise from the slight deviation in Fe_3O_4 amount and the heating process being more favorable in the compact heating beads of CS and MB than in HG. The main distinctions between the samples are the incorporation of zeolite 13× into HG and its larger bead diameter relative to the heating beads.

The presence of zeolite 13× can influence the heat treatment effects on Fe_3O_4. In particular, the water content associated with zeolite 13× can promote oxidation of Fe_3O_4 through a hydrothermal reaction pathway, converting it progressively into α-Fe_2O_3 [48,49]. Under oxidation in air at temperatures below 300°C, the oxidation rate of Fe_3O_4 is slow so that γ-Fe_2O_3 can exist as an intermediate over prolonged

Fig. 3. Image of the synthesized MAC beads: a) Homogeneous (HG), b) Core-shell (CS), c) Mixed bed (MB). The pellet of zeolite 13× used in experiments with resistive wall heating (WH) is also shown.

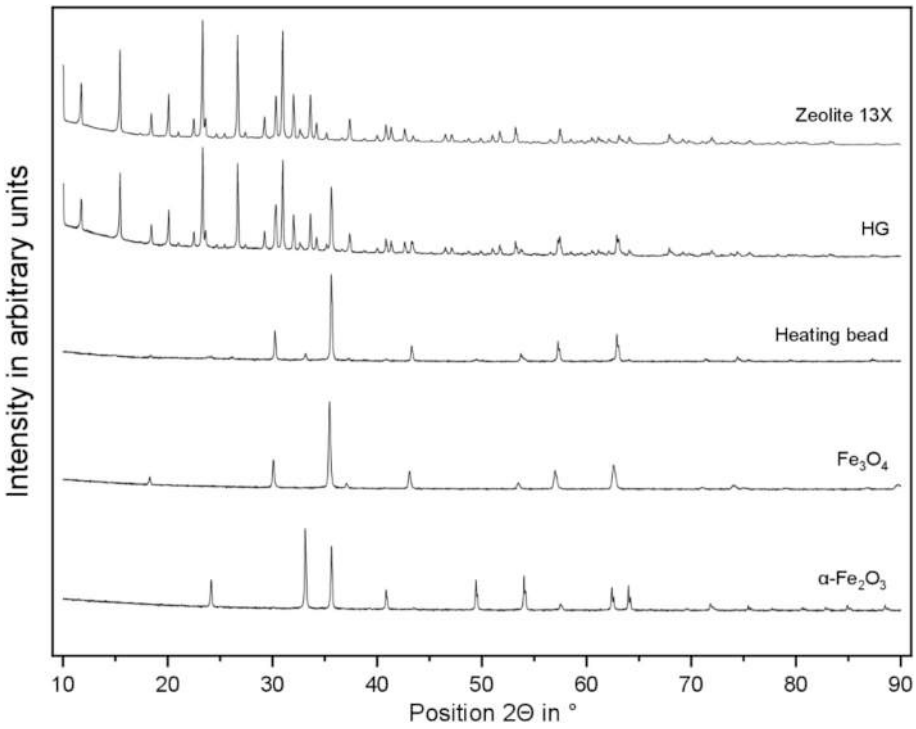

Fig. 4. Normalized XRD measurements of HG and the heating beads used in CS and MB, together with pristine zeolite 13×, Fe_3O_4 and α-Fe_2O_3.

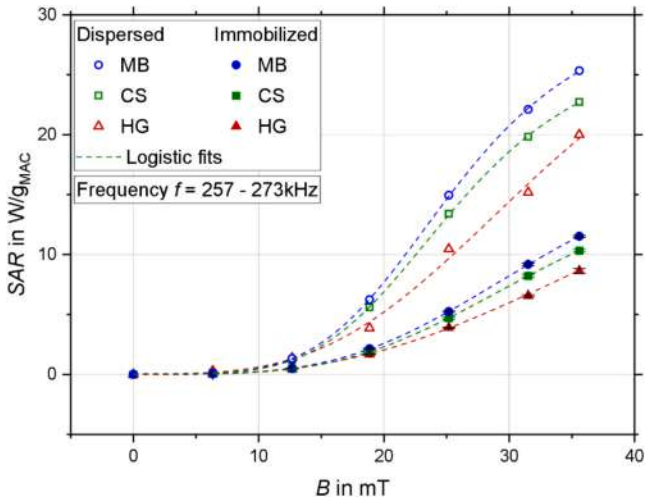

Fig. 5. Specific absorption rate (*SAR*) measurements of MB, CS and HG dispersed in water and immobilized in SiO_2 powder under different magnetic field strengths (B). *SAR* was interpolated by logistic fit.

Table 2
Material characterization of MAC. BET (surface area (A_{BET}), pore volume (V_{pore}), magnetic saturation magnetization (M_s), magnetic remanent magnetization (M_r) and coercivity (H_c).

	HG	CS	MB	Zeolite 13×
$A_{BET}/\left(\frac{m^2}{g_{MAC}}\right)$	331	304	312	560
$V_{pore}/\left(\frac{cm^3}{g_{MAC}}\right)$	0.185	0.168	0.175	0.277
$M_s/\left(\frac{emu}{g_{MAC}}\right)$	15.0	21.5	27.9	/
$M_r/\left(\frac{emu}{g_{MAC}}\right)$	1.0	1.9	2.1	/
$H_c/(Oe)$	38.0	64.5	62.5	/

time spans [48]. These effects are consistent with the reduced magnetic properties observed for HG. The formation of α-Fe_2O_3 is expected to be limited, since stronger presence would significantly diminish the magnetic response compared to Fe_3O_4 or γ-Fe_2O_3.

Fig. 5 shows different *SAR* values determined using dispersed and immobilized measurement methods. Dispersing the magnetic material in water is common practice for *SAR* measurements [25] and done in this work to be comparable with literature values. However, this approach is less representative of heat release within the solid beads, since the rotational freedom of dispersed particles enhances their apparent heating efficiency [42]. For non-nanosized magnetic particles, Néel relaxation does not contribute significantly. Brownian relaxation on the other hand, which describes the rotation of entire particles in response to the alternating magnetic field [50], depends on the viscosity of the surrounding medium [41]. In immobilized systems such as MACs, magnetic heating occurs predominantly through hysteresis losses [41]. Therefore, to represent the heat generation in the solid beads, *SAR* was additionally measured without liquid dispersion but dispersion in SiO_2 instead.

Fe_3O_4 exhibits a considerably high electrical conductivity of $\sigma_{el} = 10^2 - 10^3\ \Omega^{-1}cm^{-1}$ [51], whereas zeolite 13× is practically an electric insulator [52]. Effective eddy-current heating under induction conditions requires the electromagnetic skin depth ($\delta\ [mm]$) to be smaller than the particle radius [53]. δ for the heating bead can be estimated using Eq. (20) [53]:

$$\delta = \sqrt{\frac{2}{2\pi f \bullet \sigma_{el} \bullet \mu_0 \bullet \mu_r}} \tag{20}$$

The relative magnetic permeability μ_r of Fe_3O_4 at room temperature is approximately $\mu_r \approx 10$ [54] and decreases with increasing temperature [55]. At room temperature and $f = 257 - 273\ kHz$ (see Fig. S2), δ is $\geq 1\ mm$, and thus slightly larger than the heating bead radius. For HG, δ is expected to be even greater as the material mainly consists of non-conductive zeolite 13×, resulting in a much lower σ_{el}. Consequently, eddy current dissipation does not significantly contribute to the heating process, and the observed differences in heating performance

arise primarily from variations in the magnetic properties of the materials.

In conclusion, the produced MAC exhibited suitable pore structure and magnetic properties for inductively heated TSA. Magnetic hysteresis was identified as the main heating mechanism of the immobilized magnetic particles of the MAC. Fe_3O_4 oxidation to γ-Fe_2O_3 during the thermal treatment in air, without forming significant amounts of α-Fe_2O_3, maintained a magnetic behavior similar to that of Fe_3O_4. However, hydrothermal effects caused by moisture adsorbed on zeolite 13× likely promoted oxidation to a greater extent to α-Fe_2O_3, thereby reducing magnetic performance of HG compared to the CS and MB heating beads [32].

3.2. Heating and desorption dynamics

MACs with different structural designs were evaluated for their suitability in induction TSA using temperature-feedback control. Adsorption-desorption cycles were conducted with HG, CS, and MB at desorption setpoint temperatures of 100°*C*, 125°*C* and 150°*C*. WH experiments using P_{WH} of 5 *W* and 10 *W* served as reference cases for conventional heating, where the heat source was located outside the reactor. Additionally, RT experiments without heating were carried out to assess the influence of the N_2 flow on desorption. Adsorption-desorption cycles were conducted until a steady-state effective working capacity was reached. The steady-state of a material at one desorption temperature (T_{des} [°*C*])was reached in between 10 and 30 cycles, in average after 20 cycles, as shown in Fig. S6.The CS measurements are shown as a representative example, with the lines obtained by B-spline interpolation visualizing the trend. After drying at 125°*C*, the adsorbed CO_2 amount gradually decreased from its initial value and approached a first steady state at a desorption temperature of 100°*C* (or a resistive heating power of 5 *W*), which defines the effective working capacity at this operating point. Upon increasing the desorption temperature setpoint or the applied heating power, a new steady-state effective working capacity was established. The transient behavior is most likely caused by internal mass-transfer limitations within the beads. Due to the comparatively long diffusion path length, several adsorption-desorption cycles are required for the internal concentration profiles to fully adjust to a new operating condition and for a cyclic steady state to be established. The observed fluctuations can be attributed to residual adsorbed water, as the drying step at 125°*C* is insufficient to fully remove strongly bound moisture.

Fig. 6 presents the temperature controlled via the feedback loop, the heating magnetic field, and the desorbed CO_2 flow using HG, CS and MB with 150°*C* desorption temperature, together with WH using 10 *W*. The respective figures for WH at 5 *W* and RT are given in the SM in Figure S7and Fig. S8. From the temperature measurements the *HR* was determined from the steepest linear section of the curve.

All inductively heated cases could be successfully controlled using the manually tuned PID parameters, achieving rapid initial heating at high magnetic field strength and reaching the desired desorption temperature with limited overshoot and no sustained oscillations. Although HG exhibited slightly lower *SAR* values than CS and MB (Fig. 5), it showed the highest *HR* in Fig. 6. This can be attributed to more uniform heat distribution within the adsorbent bed and increased contact of heating material with the temperature sensor. Due to the less direct

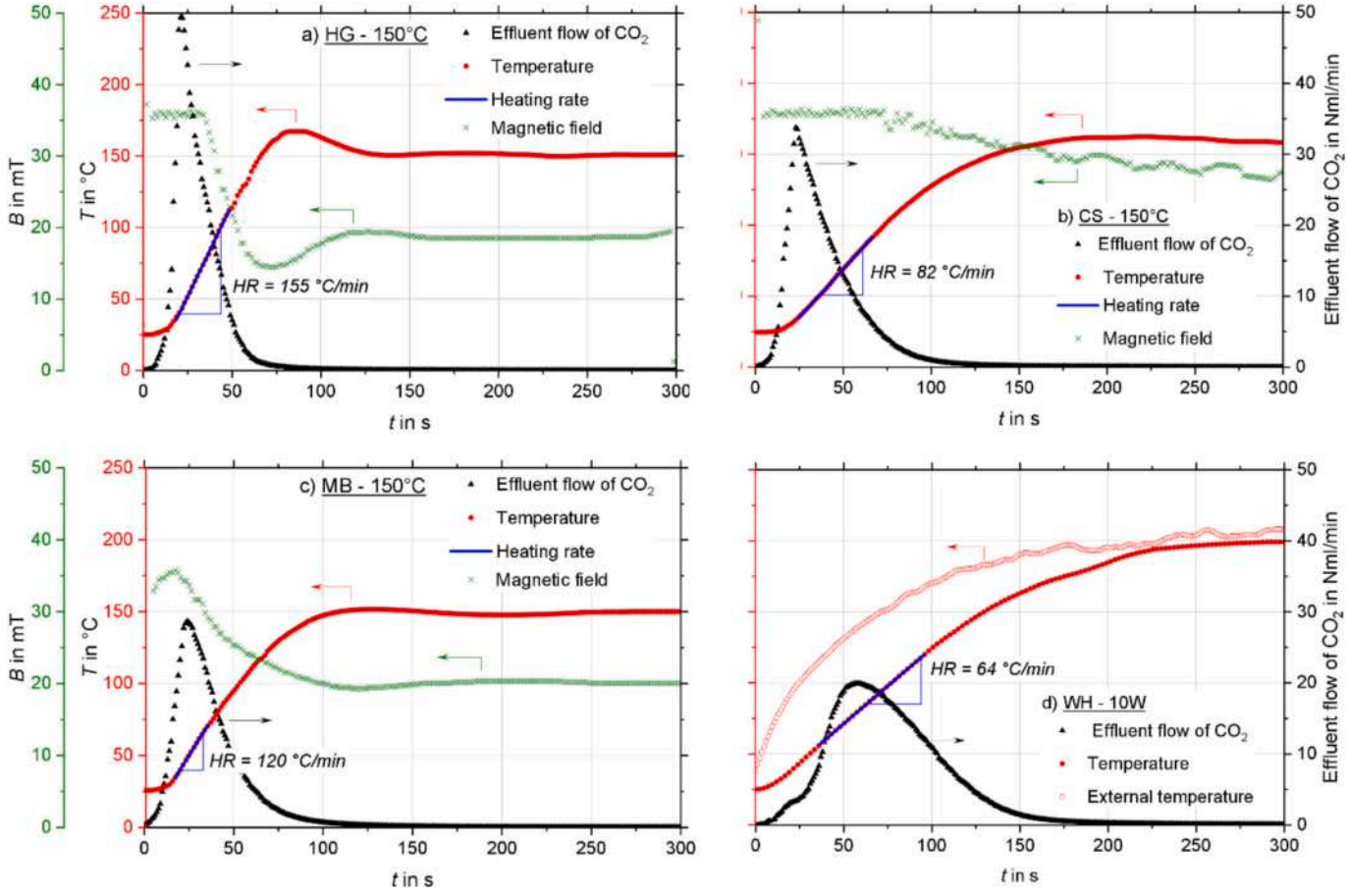

Fig. 6. Desorption dynamics of a) HG, b) CS and c) MB at 150°*C* desorption setpoint temperature together with d) WH at 10 *W*. The plots show the temperature development inside of the adsorption bed, the magnetic field strength (*B*) and the CO_2 effluent flow. The maximum heating rate (*HR*) during the experiment is displayed with every temperature curve.

heating response to the temperature sensor, the heating beads in MB and CS supposedly reached even higher temperatures than the indicated 150°C. Images of the respective materials after experiments are shown in the SM under Fig. S5. A greyish discoloration of the adsorbent beads in MB, where they were in contact with heating beads, as well as within the shell of CS, indicated localized overheating. Similarly, the adsorbent beads in the WH experiment at 10 *W* were exposed to temperatures up to 200°C and showed slight discoloring. For the long term stability (thousands of cycles) this overheating can increase the degradation rates of adsorbents such as zeolite 13× [56].

The difference in temperature control between the samples is also indicated by the magnetic field strength needed to maintain 150°C measured by the temperature sensor: MB needs a slightly higher magnetic field strength than HG, despite having a higher *SAR*. This is due to a less homogeneous temperature throughout the MB. In that aspect, the slow temperature response of CS through the shell leads to a significantly higher steady state magnetic field strength. In the WH experiment at 10 *W*, *HR* of the heating wire on the outside of the reactor was higher than by induction heating. Nevertheless, *HR* inside of the adsorption bed was significantly lowered, due to the heat conduction through the reactor wall. Furthermore, it can be observed how the desorption in WH experiments was initially driven by the N_2 stream until the elevated temperature contributed to the CO_2 desorption (see results for RT desorption (Fig. S8)). Inductively heated TSA exhibited a markedly sharper CO_2 effluent peak compared to WH. HG had the minimal extent of effluent flow tailing. HG showed the least tailing, meaning that most of the CO_2 was desorbed in a short period for a less significant N_2 amount. This is particularly advantageous, as it enables high product purity without substantially reducing recovery, which is a trade-off in TSA systems where prolonged desorption increases nitrogen dilution. Comparing the desorption time, HG yielded the fastest desorption (94 *s*), followed by CS (142 *s*), MB (146 *s*) and WH at 10 W (225 *s*). In all inductively heated cases, the temperature setpoint was reached when the desorption was almost completed, although most CO_2 had already been released by that point.

From a heat and mass transfer perspective, the effect of homogeneous heating can be understood by comparing CS and HG beads. The internal temperature distribution within the bead directly affects diffusion-controlled transport of CO_2 from the porous adsorbent to the gas phase. In CS beads, the heating material is concentrated in the core and surrounded by a thermally insulating zeolite 13× shell, which is expected to produce a larger radial temperature gradient than in HG beads for the same energy input. At the bead surface, purge-gas flow lowers the CO_2 partial pressure and promotes desorption, as also observed under RT desorption conditions (Fig. S8). While CO_2 adsorbed near the bead surface experiences short diffusion paths, CO_2 located deeper inside the bead must diffuse over longer distances and would, in principle, benefit from elevated internal temperatures. For CS beads, this could theoretically result in faster desorption and reduced tailing. However, the experimentally observed behavior shows slower desorption and increased tailing for CS compared to HG, indicating that the shell thickness is too large. Delayed heat conduction toward the outer shell region limits the temperature rise there, slowing diffusion and desorption. In contrast, HG beads benefit from more uniform and rapid heating throughout the adsorbent volume, resulting in faster desorption and reduced tailing. These findings highlight the importance of fast heating and carefully designed adsorbents in TSA processes, particularly given the low thermal conductivity of CO_2 adsorbents like zeolite 13× [21].

3.3. Working capacity

The effective working capacity was determined by performing repeated adsorption-desorption cycles until a steady state was achieved. The relative error of the Δq_{CO_2} at steady-state was $\varepsilon < 2.0\%$. Fig. 7 compares the experimentally measured working capacity of the different MACs under the respective desorption temperature setpoint. Furthermore, the $E_{heating}$ released during each respective desorption is shown to account for the energetical effectiveness of each desorption strategy.

As expected, higher desorption temperatures increased both the effective working capacity as well as $E_{heating}$. Inductively heated adsorbents require significantly lower $E_{heating}$ for the same effective working capacity compared to WH. Among all cases, WH at 10 *W* reached the highest effective working capacity due to the highest temperature reached and the absence of non-adsorptive magnetic material. The $E_{heating}$ for WH at both, 5 *W* and 10 *W*, was significantly higher than for any inductively heated desorption. $E_{heating}$ of WH at 5 *W*, which reached around 125°C (see Fig. S7), was between 2 and 5 times higher than the induction heated experiments at 125°C. It should be noted that the en-

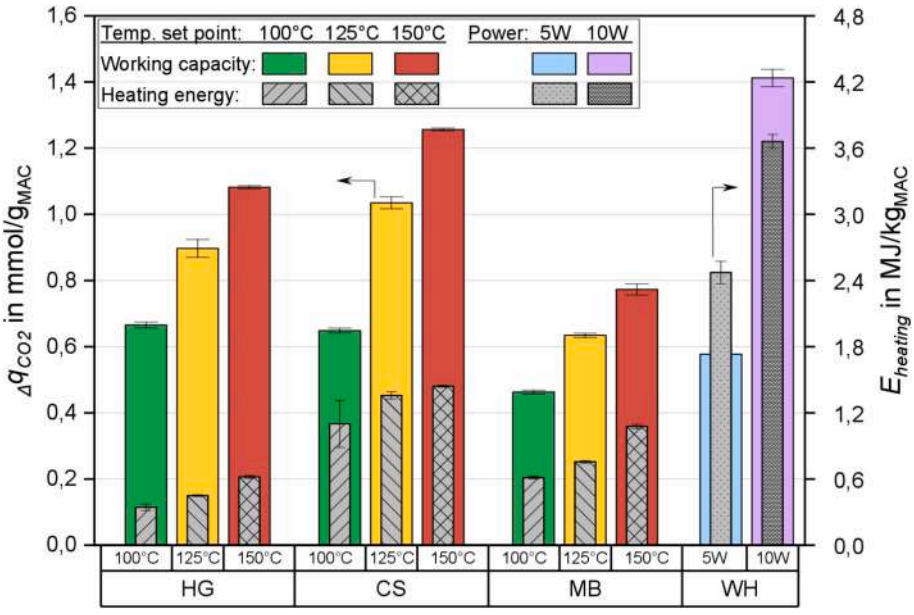

Fig. 7. Effective working capacity (Δq_{CO_2}) of HG, CS and MB for different setpoint temperatures together with WH at different powers. The heating energy $(E_{heating})$ released during each respective desorption is plotted for comparison.

ergy required to generate the magnetic field can be higher than $E_{heating}$ due to imperfect coupling of the magnetic field and the magnetic particles. Fig. 7 therefore shows the potential of induction heating for electrifying TSA processes in comparison to the limitations of externally heated processes. Using induction heating, CS achieved the highest effective working capacity of 1.26 $\frac{mmol}{g_{MAC}}$, followed by HG with 1.08 $\frac{mmol}{g_{MAC}}$, while HG required only about 40% of the $E_{heating}$ consumed by CS. In contrast, MB exhibited the lowest effective working capacity of 0.77 $\frac{mmol}{g_{MAC}}$ with a heating energy consumption between HG and CS. It should be noted that $E_{heating}$ during induction heating accounts for the energy released in the bead, while for WH it accounts for the total energy spent.

RT desorption, driven only by N_2 flow, required with $t_{des} \approx 20\ min$ around 12 times longer than HG at 150°C (see Fig. S8). Consequently, RT desorption results in a product of significantly lower purity and is therefore not a practical option.

At 100°C and 125°C, CS showed $E_{heating}$ values similar to those at 150°C, while HG and MB exhibited greater differences between 100°C, 125°C and 150°C setpoint temperature. This reflects the challenge of controlling a rapidly responding TSA system using a temperature feedback loop when response delays are present. The temperature control approach is therefore more suitable for systems with direct and immediate thermal response, such as HG or MB.

3.4. Evaluation of the regeneration energy

The performance of the MAC in this work was compared with literature materials that were also tested under inert purge gas flow. Table 3 compares the regeneration energy ($E_{reg,min}$) as the theoretical minimum energy required to desorb the adsorbed CO_2 and the productivity of the inductively heated materials studied in this work and the literature.

HG outperformed CS and MB by a 35% faster desorption through a steeper desorption curve and less tailing, while having the same and higher effective working capacity, which resulted in the highest productivity comparing results at 150°C desorption temperature. Although HG showed similar $E_{reg,min}$ values across different temperature setpoints, its productivity increased remarkably from 0.23 $\frac{mg_{CO_2}}{g_{MAC} \cdot s}$ at $T_{des} = 100^{\circ}C$ to 0.52 $\frac{mg_{CO_2}}{g_{MAC} \cdot s}$ at $T_{des} = 150^{\circ}C$. Especially for CS and MB the temperature of the heating bead was supposedly higher.

Sadiq et al. [18] reported a homogeneous MAC powder composed of $MgFe_2O_4$ as the heating material and Mg-MOF-74 as the adsorbent. Due to the extremely high adsorption capacity of Mg-MOF-74 ($q_{CO_2} = 6.28$ at $T = 25^{\circ}C$ and $p_{CO_2} = 15\ kPa$ [18]) they obtained a productivity of 0.68 $\frac{mg_{CO_2}}{g_{MAC} \cdot s}$ and $E_{reg,min} = 2.77$ $\frac{MJ}{kg_{CO_2}}$ at $T_{des} = 130^{\circ}C$ which are values slightly higher to the MACs synthesized in this work. However, it should be noted that the $MgFe_2O_4$/Mg-MOF-74 composite was only tested in powder form and was not subjected to repeated adsorption-desorption cycles to reach steady-state effective working capacity. In comparison, a powder mixture of Fe_3O_4 and HKust-1 exhibited lower productivity and higher $E_{reg,min}$, than the MACs of this work [19]. Furthermore, the MACs in this work were dried at 120°C under N_2 flow, which preserved the comparability between the samples, but most likely did not desorb strongly adsorbed moisture. In the comparing literature, materials were tested either using a flow-through gas adsorption apparatus (Micromeritics AutoChem II 2920) without referring to the drying process [19] or using adsorption isotherms [18].

3.5. Energy efficiency

For a low-energy-demand CO_2 TSA process, the energy expenditure compared to the captured CO_2 amount is important. Therefore, the distribution of the electrical grid energy during desorption was analyzed. Fig. 8 presents the stacked, CO_2 specific energy distribution, being t he minimum required regeneration energy ($E_{reg,min}$) as well as thermal ($E_{loss,th}$) and electrical ($E_{loss,el}$) losses.

The distribution of electrical grid energy during desorption highlights both the potential and the current limitations of induction-heated CO_2 TSA. The numerical values of the energy distribution are provided in Table S4 in the SM.

In this study, the electrical grid energy consumed exceeded the minimum regeneration energy (2.5 – 3.9 $\frac{MJ}{kg_{CO_2}}$) for all heating methods. WH required 60 – 100 $\frac{MJ}{kg_{CO_2}}$, whereas induction heating demanded substantially higher grid energies, ranging from approximately 200 up to 1200 $\frac{MJ}{kg_{CO_2}}$. The key difference is the nature of the losses. In induction heating, more than 95% of the grid energy loss was attributed to electrical losses associated with magnetic field coupling to the MAC, while for WH the losses were thermal. It should be noted that the here presented system was build in a scale that did not favor efficient magnetic field coupling, but a non-disturbed magnetic field to ensure compara-

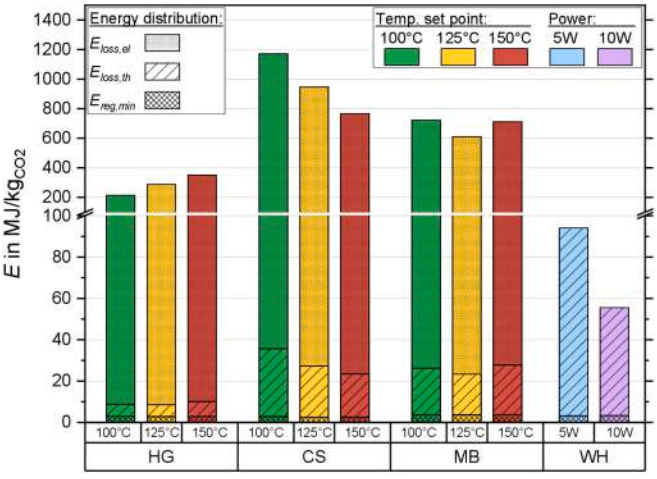

Fig. 8. Energy distribution of the consumed grid energy during desorption of HG, CS and MB for different setpoint temperatures together with WH at different powers. The Energy is distributed into the minimum regeneration energy ($E_{reg,min}$), the thermal ($E_{loss,th}$) and electrical ($E_{loss,el}$) losses.

Table 3
Comparison of the theoretical minimum regeneration energy ($E_{reg,min}$) and productivity of the materials studied in this work with literature.

Material	Structure	T_{des}/(°C)	$E_{reg,min}/\left(\frac{MJ}{kg_{CO_2}}\right)$	Productivity/$\left(\frac{mg_{CO_2}}{g_{MAC} \cdot s}\right)$	Source
Fe_3O_4/zeolite 13×	HG	100	2.95	0.23	This work
Fe_3O_4/zeolite 13X	HG	125	2.83	0.43	This work
Fe_3O_4/zeolite 13X	HG	150	2.91	0.52	This work
Fe_3O_4/zeolite 13X	CS	150	2.59*	0.38	This work
Fe_3O_4/zeolite 13X	MB	150	3.86	0.23	This work
$MgFe_2O_4$/Mg-MOF-74	Powder	130	2.77	0.68	[18]
Fe_3O_4/HKust-1	Powder	130	4.40	0.38	[19]

* Temperature side of the bead was supposedly higher than the measured bed temperature.

bility.

When considering only the thermal energy available to the system, induction heating outperformed WH in terms of heat utilization for CO_2 desorption. Among the investigated MAC designs, HG exhibited the lowest thermal losses and the highest thermal efficiency, reaching approximately 25%, compared to a maximum of about 6% for WH. The lower thermal losses of induction heating reflect its internal heat generation, whereas WH suffers from significant losses due to heating of the entire column and limited heat transfer through the column walls and the packed bed. These limitations are strongly influenced by column geometry and packing density, to which WH is more sensitive than inductively heated MACs.

For the present setup, the relatively large bead size compared to the column diameter prevented close packing and reduced wall contact. While this penalizes WH performance, the small column diameter used here favored it. Increasing column diameter during scale-up would reduce the surface-to-volume ratio and increase thermal WH losses. In contrast, internal heat generation by induction heating is not subject to these geometric constraints, although maintaining comparable magnetic field conditions during scale-up represents a critical challenge.

Improving overall energy efficiency therefore requires minimizing both electrical and thermal losses. As shown by the coupled heating and desorption dynamics (Fig. 6), CO_2 desorption was nearly complete upon reaching the maximum temperature, while continued heating during the tailing phase resulted in high energy input with diminishing CO_2 release. In such cases, where desorption becomes pore-diffusion-limited while the CO_2 has already desorbed from the adsorbent's surface, terminating heating earlier could substantially improve efficiency.

Further reductions in electrical losses will require optimization of magnetic field coupling, including coordinated adjustment of MAC loading, coil geometry, and coil dimensions. Thermal losses can be further reduced by rapid heating, as shown by the HG-MAC, and by increasing column diameter, which lowers the surface-to-volume ratio. At those high heating rates however, the column dimensions and geometry must be balanced against the emerging bottleneck of the cooling step, which limits cycle time. In contrast, WH is inherently more constrained by increasing column diameter, underlining the advantages of induction heating for scalable TSA operation.

4. Conclusions

MACs consisting of Fe_3O_4 as the heating material and zeolite 13× as the adsorbent were evaluated for their suitability in inductively heated TSA CO_2 capture using a temperature feedback-loop control to study the influence of the desorption temperature (T_{des}). Three MAC configurations were tested: A homogeneous mixture (HG) of the functional powders, a core-shell design (CS) with an Fe_3O_4 heating bead as core and a zeolite 13× shell, and a mixed bed configuration (MB) in which adsorbent and heating beads were placed separately in the reactor. As a conventional TSA reference, adsorbent beads of zeolite 13× without Fe_3O_4 were desorbed using resistive wall heating (WH). Additionally, desorption at room temperature (RT) was performed to evaluate the influence of the N_2 stripping gas. Adsorption-desorption cycles were conducted until steady-state conditions were reached. The materials were compared based on their steady-state effective working capacity (Δq_{CO_2}), desorption profiles, minimal regeneration energy ($E_{reg,min}$) and energy efficiency, respectively.

Among the studied materials, HG demonstrated the best overall performance, exhibiting a fast thermal response to temperature feedback control, a high HR (155 $\frac{^\circ C}{min}$) and good Δq_{CO_2}(1.08 $\frac{mmol}{g_{MAC}}$). These characteristics resulted in a steep desorption curve, with 99% of CO_2 desorbed within 94 s and the highest productivity of 0.52 $\frac{mg_{CO_2}}{g_{MAC} \cdot s}$ at a thermal energy efficiency of 25%. The corresponding $E_{reg,min}$ was below 3.0 $\frac{MJ}{kg_{CO_2}}$, which is close to the values reported for Mg-MOF-74-based composites.

The functional separation of the MAC into an adsorbent shell and a heating core provided the highest Δq_{CO_2} (1.26 $\frac{mmol}{g_{MAC}}$) but also resulted in an increased energy consumption and did not demonstrate a clear advantage over HG or MB. Temperature feedback control in CS was hindered by limited heat conduction through the shell. Although this effect might be mitigated by using thinner shells, HG already exhibited highly effective desorption dynamics. This was observed even though HG showed a slightly reduced energy release under the applied magnetic field strength (i.e. lower SAR), compared to the CS and MB.

Compared with resistive wall heated TSA, the inductively heated system exhibited significantly higher thermal efficiency, due to the inherently inefficient heat transfer of WH across the reactor wall and adsorbent bed. However, the total grid energy of induction heating was substantially higher in induction heating due electric energy losses of incomplete magnetic field coupling with the magnetic material.

Overall, this study demonstrates the potential of induction heating to outperform conventional heating in TSA processes, owing to its localized and rapid heat generation, but also its challenge to convert the grid energy into heating energy. Future research should focus on improving the overall efficiency of the induction system by optimizing the conversion of electrical energy input into heating energy released within the MAC.

CRediT authorship contribution statement

Oliver Stratil: Investigation, Conceptualization, Methodology, Writing – original draft. **Oscar Cespedes:** Formal analysis, Resources, Writing – review & editing. **Olivier Croquet:** Formal analysis, Resources, Writing – review & editing. **Thierry Visart de Bocarmé:** Formal analysis, Resources, Writing – review & editing. **Rafael Gonzalez-Olmos:** Writing – review & editing, Supervision. **Javier Fernandez-Garcia:** Visualization, Conceptualization, Software, Writing – review & editing, Funding acquisition, Supervision.

Declaration of competing interest

The authors declare no competing interests.

Acknowledgements

The financial support of this work by the funding bodies AGAUR (2021 BP 00029, 2023 PROD 00004 and LLAV 2024 00060) is gratefully acknowledged. This research is also supported by project RE(*F*)CICLA (PID2023-149713OB-I00) funded by the Spanish Ministry of Science, Innovation and Universities. Recognition from AGAUR as Consolidated Research Groups for GESPA (2021 SGR 00321) is gratefully appreciated.

Appendix A. Supplementary data

Supplementary data to this article can be found online at https://doi.org/10.1016/j.cej.2026.174901.

Data availability

Data will be made available on request.

References

[1] Intergovernmental Panel on Climate Change (IPCC), Climate Change 2021: The Physical Science Basis, 2021.

[2] S. Zhang, Y. Shen, C. Zheng, Q. Xu, Y. Sun, M. Huang, L. Li, X. Yang, H. Zhou, H. Ma, Z. Li, Y. Zhang, W. Liu, X. Gao, Recent advances, challenges, and perspectives on carbon capture, Front. Environ. Sci. Eng. China 18 (2024) 75, https://doi.org/10.1007/s11783-024-1835-0.

[3] S. Bouckaert, A. Fernandez Pales, C. McGlade, U. Remme, B. Wanner, in: International Energy Agency (Ed.), Net Zero by 2050 - a Roadmap for the Global Energy Sector, 2021.

[4] E. Benhelal, G. Zahedi, E. Shamsaei, A. Bahadori, Global strategies and potentials to curb CO2 emissions in cement industry, J. Clean. Prod. 51 (2013) 142–161, https://doi.org/10.1016/j.jclepro.2012.10.049.

[5] L. Holappa, A general vision for reduction of energy consumption and CO2 emissions from the steel industry, Metals (Basel). 10 (2020) 1117, https://doi.org/10.3390/met10091117.

[6] P. Bains, P. Psarras, J. Wilcox, CO 2 capture from the industry sector, Prog. Energy Combust. Sci. 63 (2017) 146–172, https://doi.org/10.1016/j.pecs.2017.07.001.

[7] H. Majeed, H.F. Svendsen, Characterization of aerosol emissions from CO2 capture plants treating various power plant and industrial flue gases, Int. J. Greenh. Gas Con. 74 (2018) 282–295, https://doi.org/10.1016/j.ijggc.2018.04.016.

[8] M. Bui, C.S. Adjiman, A. Bardow, E.J. Anthony, A. Boston, S. Brown, P.S. Fennell, S. Fuss, A. Galindo, L.A. Hackett, J.P. Hallett, H.J. Herzog, G. Jackson, J. Kemper, S. Krevor, G.C. Maitland, M. Matuszewski, I.S. Metcalfe, C. Petit, G. Puxty, J. Reimer, D.M. Reiner, E.S. Rubin, S.A. Scott, N. Shah, B. Smit, J.P.M. Trusler, P. Webley, J. Wilcox, N. Mac Dowell, Carbon capture and storage (CCS): the way forward, Energy Environ. Sci. 11 (2018) 1062–1176, https://doi.org/10.1039/C7EE02342A.

[9] D. Bahamon, L.F. Vega, Systematic evaluation of materials for post-combustion CO2 capture in a temperature swing adsorption process, Chem. Eng. J. 284 (2016) 438–447, https://doi.org/10.1016/j.cej.2015.08.098.

[10] A. Gutierrez-Ortega, R. Nomen, J. Sempere, J.B. Parra, M.A. Montes-Morán, R. Gonzalez-Olmos, A fast methodology to rank adsorbents for CO2 capture with temperature swing adsorption, Chem. Eng. J. 435 (2022) 134703, https://doi.org/10.1016/j.cej.2022.134703.

[11] R.T. Yang, Adsorbents: fundamentals and applications, Wiley, 2003, https://doi.org/10.1002/047144409X.

[12] D. Ko, M. Kim, I. Moon, D. Choi, Analysis of purge gas temperature in cyclic TSA process, Chem. Eng. Sci. 57 (2002) 179–195, https://doi.org/10.1016/S0009-2509(01)00358-X.

[13] M. Schoukens, M. Gholami, G.V. Baron, T. Van Assche, J.F.M. Denayer, Hybrid induction vacuum swing adsorption, a rapid and fully electrified carbon capture process, Chem. Eng. J. 459 (2023), https://doi.org/10.1016/j.cej.2023.141587.

[14] J. Merel, M. Clausse, F. Meunier, Experimental investigation on CO $_2$ post−combustion capture by indirect thermal swing adsorption using 13X and 5A zeolites, Ind. Eng. Chem. Res. 47 (2008) 209–215, https://doi.org/10.1021/ie071012x.

[15] C. Ellison, J. Hoffman, D. Shekhawat, Comparison of microwave and conventional heating for CO2 desorption from zeolite 13X, Int. J. Greenh. Gas Con. 107 (2021), https://doi.org/10.1016/j.ijggc.2021.103311.

[16] M. Songolzadeh, M. Soleimani, M. Takht Ravanchi, R. Songolzadeh, Carbon dioxide separation from flue gases: a technological review emphasizing reduction in greenhouse gas emissions, Sci. World J. 2014 (2014) 1–34, https://doi.org/10.1155/2014/828131.

[17] J. Shi, T. Zhang, S. Sun, L. Gong, Ab initio insights into the CO2 adsorption mechanisms in hydrated silica nanopores, Chem. Eng. Sci. 313 (2025) 121741, https://doi.org/10.1016/j.ces.2025.121741.

[18] M.M. Sadiq, K. Konstas, P. Falcaro, A.J. Hill, K. Suzuki, M.R. Hill, Engineered porous nanocomposites that deliver remarkably low carbon capture energy costs, Cell Rep. Phys. Sci. 1 (2020), https://doi.org/10.1016/j.xcrp.2020.100070.

[19] M. Bellusci, M. Albino, A. Masi, D. Peddis, C. Innocenti, F. Varsano, High porosity-magnetic composite materials for magnetic induction swing adsorption (MISA): improvement of performance properties, Mater. Chem. Phys. 311 (2024) 128525, https://doi.org/10.1016/j.matchemphys.2023.128525.

[20] L. Sun, B. Liao, D. Sheberla, D. Kraemer, J. Zhou, E.A. Stach, D. Zakharov, V. Stavila, A.A. Talin, Y. Ge, M.D. Allendorf, G. Chen, F. Léonard, M. Dincă, A microporous and naturally nanostructured thermoelectric metal-organic framework with ultralow thermal conductivity, Joule 1 (2017) 168–177, https://doi.org/10.1016/j.joule.2017.07.018.

[21] K.C. Chan, C.Y.H. Chao, M. Bahrami, Heat and mass transfer characteristics of a zeolite 13X/CaCl2 composite adsorbent in adsorption cooling systems, in: ASME 2012 6th International Conference on Energy Sustainability, Parts a and B, American Society of Mechanical Engineers, 2012, pp. 49–58, https://doi.org/10.1115/ES2012-91246.

[22] S.E. Zanco, M. Ambrosetti, G. Groppi, E. Tronconi, M. Mazzotti, Heat transfer intensification with packed open-cell foams in TSA processes for CO2 capture, Chem. Eng. J. 430 (2022) 131000, https://doi.org/10.1016/j.cej.2021.131000.

[23] D. Marx, L. Joss, M. Hefti, M. Mazzotti, Temperature swing adsorption for Postcombustion CO $_2$ capture: single- and multicolumn experiments and simulations, Ind. Eng. Chem. Res. 55 (2016) 1401–1412, https://doi.org/10.1021/acs.iecr.5b03727.

[24] F. Berg, C. Pasel, T. Eckardt, D. Bathen, Temperature swing adsorption in natural gas processing: a concise overview, ChemBioEng Reviews 6 (2019) 59–71, https://doi.org/10.1002/cben.201900005.

[25] M. Gholami, B. Verougstraete, R. Vanoudenhoven, G.V. Baron, T. Van Assche, J.F. M. Denayer, Induction heating as an alternative electrified heating method for carbon capture process, Chem. Eng. J. 431 (2022), https://doi.org/10.1016/j.cej.2021.133380.

[26] Vimal R. Nakum, Kevin M. Vyas, N.C. Mehta, RESEARCH ON INDUCTION HEATING - A REVIEW, Int. J. Sci. Eng. Appl. 02 (2013) 141–144, https://doi.org/10.7753/IJSEA0206.1005.

[27] B. Verougstraete, M. Gholami, Y. Gomez-Rueda, E. Pérez-Botella, M. Schoukens, T. R.C. Van Assche, J.F.M. Denayer, Advancements and challenges in electric heating for enhanced temperature swing adsorption processes, Sep. Purif. Technol. 353 (2025) 128522, https://doi.org/10.1016/j.seppur.2024.128522.

[28] H. Li, M.M. Sadiq, K. Suzuki, R. Ricco, C. Doblin, A.J. Hill, S. Lim, P. Falcaro, M. R. Hill, Magnetic metal-organic frameworks for efficient carbon dioxide capture and remote trigger release, Adv. Mater. 28 (2016) 1839–1844, https://doi.org/10.1002/adma.201505320.

[29] W. Wang, G. Tuci, C. Duong-Viet, Y. Liu, A. Rossin, L. Luconi, J.-M. Nhut, L. Nguyen-Dinh, C. Pham-Huu, G. Giambastiani, Induction heating: an enabling Technology for the Heat Management in catalytic processes, ACS Catal. 9 (2019) 7921–7935, https://doi.org/10.1021/acscatal.9b02471.

[30] K. Newport, K. Baamran, A.A. Rownaghi, F. Rezaei, Magnetic-field assisted gas desorption from Fe2O3/zeolite 13X sorbent monoliths for biogas upgrading, Ind. Eng. Chem. Res. 61 (2022) 18843–18853, https://doi.org/10.1021/acs.iecr.2c02969.

[31] K.L. Pisane, Effects of Size and Size Distribution on the Magnetic Properties of Maghemite Nanoparticles and Iron-Platinum Core-Shell Nanoparticles, West Virginia University, 2010.

[32] R.M. Cornell Schwertmann Udo., the iron Oxides : Structure, Properties, Reactions, Occurrences, and Uses, Wiley-VCH, 2003.

[33] H. Li, M.M. Sadiq, K. Suzuki, P. Falcaro, A.J. Hill, M.R. Hill, Magnetic induction framework synthesis: a general route to the controlled growth of metal-organic frameworks, Chem. Mater. 29 (2017) 6186–6190, https://doi.org/10.1021/acs.chemmater.7b01803.

[34] B. He, M.M. Sadiq, M.P. Batten, K. Suzuki, M. Rubio-Martinez, J. Gardiner, M. R. Hill, Continuous flow synthesis of a Zr magnetic framework composite for post-combustion CO2 capture, Chem. Eur. J. 25 (2019) 13184–13188, https://doi.org/10.1002/chem.201902560.

[35] N. Tlili, G. Grévillot, C. Vallières, Carbon dioxide capture and recovery by means of TSA and/or VSA, Int. J. Greenh. Gas Con. 3 (2009) 519–527, https://doi.org/10.1016/j.ijggc.2009.04.005.

[36] M.M. Sadiq, H. Li, A.J. Hill, P. Falcaro, M.R. Hill, K. Suzuki, Magnetic induction swing adsorption: an energy efficient route to porous adsorbent regeneration, Chem. Mater. 28 (2016) 6219–6226, https://doi.org/10.1021/acs.chemmater.6b02409.

[37] C. Shen, C.A. Grande, P. Li, J. Yu, A.E. Rodrigues, Adsorption equilibria and kinetics of CO2 and N2 on activated carbon beads, Chem. Eng. J. 160 (2010) 398–407, https://doi.org/10.1016/j.cej.2009.12.005.

[38] Z. Zhao, Z. Li, Y.S. Lin, Adsorption and diffusion of carbon dioxide on metal−organic framework (MOF-5), Ind. Eng. Chem. Res. 48 (2009) 10015–10020, https://doi.org/10.1021/ie900665f.

[39] X. Lin, B. Shao, J. Zhu, F. Pan, J. Hu, M. Wang, H. Liu, In situ electromagnetic induction heating for CO2Temperature swing adsorption on magnetic Fe3O4/N-doped porous carbon, Energy Fuel 34 (2020) 14439–14446, https://doi.org/10.1021/acs.energyfuels.0c02699.

[40] M. EL-SAKHAWY, H.-A.S. TOHAMY, A. SALAMA, S. KAMEL, Thermal properties of CARBOXYMETHYL cellulose acetate butyrate, Cellul. Chem. Technol. 53 (2019) 667–675, https://doi.org/10.35812/CelluloseChemTechnol.2019.53.65.

[41] A. Jordan, P. Wust, H. Fähling, W. John, A. Hinz, R. Felix, Inductive heating of ferrimagnetic particles and magnetic fluids: physical evaluation of their potential for hyperthermia, Int. J. Hyperth. 9 (1993) 51–68, https://doi.org/10.3109/02656739309061478.

[42] C.M. Lucaciu, S. Nitica, I. Fizesan, L. Filip, L. Bilteanu, C. Iacovita, Enhanced magnetic hyperthermia performance of zinc ferrite nanoparticles under a parallel and a transverse Bias DC magnetic field, Nanomaterials 12 (2022) 3578, https://doi.org/10.3390/nano12203578.

[43] D.J. Griffiths, Introduction to electrodynamics, Cambridge University Press, 2023, https://doi.org/10.1017/9781009397735.

[44] E. Tiesinga, P.J. Mohr, D.B. Newell, B.N. Taylor, CODATA recommended values of the fundamental physical constants: 2018, Rev. Mod. Phys. 93 (2021) 025010, https://doi.org/10.1103/RevModPhys.93.025010.

[45] P. Li, F.H. Tezel, Equilibrium and kinetic analysis of CO2–N2 adsorption separation by concentration pulse chromatography, J. Colloid Interface Sci. 313 (2007) 12–17, https://doi.org/10.1016/j.jcis.2007.04.015.

[46] A. Ntiamoah, J. Ling, P. Xiao, P.A. Webley, Y. Zhai, CO $_2$ capture by temperature swing adsorption: use of hot CO $_2$ -Rich gas for regeneration, Ind. Eng. Chem. Res. 55 (2016) 703–713, https://doi.org/10.1021/acs.iecr.5b01384.

[47] M. Thommes, K. Kaneko, A.V. Neimark, J.P. Olivier, F. Rodriguez-Reinoso, J. Rouquerol, K.S.W. Sing, Physisorption of gases, with special reference to the evaluation of surface area and pore size distribution (IUPAC technical report), Pure Appl. Chem. 87 (2015) 1051–1069, https://doi.org/10.1515/pac-2014-1117.

[48] Z. Li, C. Chanéac, G. Berger, S. Delaunay, A. Graff, G. Lefèvre, Mechanism and kinetics of magnetite oxidation under hydrothermal conditions, RSC Adv. 9 (2019) 33633–33642, https://doi.org/10.1039/C9RA03234G.

[49] S. Nasrazadani, A. Raman, The application of infrared spectroscopy to the study of rust systems—II. Study of cation deficiency in magnetite (Fe3O4) produced during its transformation to maghemite (γ-Fe2O3) and hematite (α-Fe2O3), Corros. Sci. 34 (1993) 1355–1365, https://doi.org/10.1016/0010-938X(93)90092-U.

[50] M. Hanson, The frequency dependence of the complex susceptibility of magnetic liquids, J. Magn. Magn. Mater. 96 (1991) 105–113, https://doi.org/10.1016/0304-8853(91)90617-J.

[51] L. Blaney, Magnetite (Fe3O4)properties, synthesis and applications, Lehigh Rev. 15 (2007).

[52] M.J. Regufe, A.F.P. Ferreira, J.M. Loureiro, A. Rodrigues, A.M. Ribeiro, Development of hybrid materials with activated carbon and zeolite 13X for CO2Capture from flue gases by electric swing adsorption, Ind. Eng. Chem. Res. 59 (2020) 12197–12211, https://doi.org/10.1021/acs.iecr.0c00184.

[53] J. Delacroix, P. Piluso, N. Chikhi, P. Fouquart, Induction heating of cylindrical loads of arbitrary skin-depth by “current-sheet” inductors, Electr. Eng. 100 (2018) 811–822, https://doi.org/10.1007/s00202-017-0557-8.
[54] K. Iwauchi, Y. Kita, N. Koizumi, Magnetic and dielectric properties of Fe $_3$ O $_4$, J. Phys. Soc. Jpn. 49 (1980) 1328–1335, https://doi.org/10.1143/JPSJ.49.1328.
[55] D. Levy, R. Giustetto, A. Hoser, Structure of magnetite (Fe3O4) above the curie temperature: a cation ordering study, Phys. Chem. Miner. 39 (2012) 169–176, https://doi.org/10.1007/s00269-011-0472-x.
[56] J.H. Jacobs, C.E. Deering, R. Sui, K.L. Lesage, R.A. Marriott, Degradation of desiccants in temperature swing adsorption processes: the temperature dependent degradation of zeolites 4a, 13x and silica gels, SSRN Electron. J. (2022), https://doi.org/10.2139/ssrn.4151358.